RSC Advances

PAPER

View Article Online
View Journal | View Issue

Cite this: *RSC Adv.*, 2023, **13**, 25316

Elucidating an efficient super-capacitive response of a $Sr_2Ni_2O_5$/rGO composite as an electrode material in supercapacitors

Farooq Ahmad, [ac] Muhammad Ahmed Khan,[a] Umer Waqas,[a] Shahid M. Ramay[b] and Shahid Atiq *[a]

Mixed transition metal oxides have emerged as efficient electrode materials because of their significant cycling stability, and superior capacitance values, resulting in remarkable electrochemical outputs. In this regard, $Sr_2Ni_2O_5$/rGO composites were synthesized using a facile solvothermal method to achieve efficient electrochemical pursuits. X-ray diffraction confirmed the formation of finely crystallized samples with the phase evolution from orthorhombic to hexagonal. Morphological studies using field emission scanning electron microscopy depicted the desired porosity in samples with well-defined shapes and sizes of homogeneously distributed grains. Elemental analysis verified the pictorial depiction of sample compositions in terms of their stoichiometric ratios. The composite sample with composition $Sr_2Ni_2O_5$@15%rGO exhibited superior electrochemical performance compared to other samples, depicting the highest specific capacitance of 148.09 F g^{-1} at a lower scan rate of 0.005 V s^{-1} observed *via* cyclic voltammetry. In addition, the cyclability performance of $Sr_2Ni_2O_5$@15%rGO exhibits 68.5% capacitive retention after 10 000 cycles. The energy density as determined using a two-electrode system remained 4.375 W h kg^{-1} for the first cycle which reduced to 1.875 W h kg^{-1} for the 10 000th cycle, with a maximum power density of 1.25 W kg^{-1}. The Nyquist plot represented less barrier to charge transfer. The electrode with particular composition $Sr_2Ni_2O_5$@15%rGO emerged as significant, exhibiting a superior surface capacitive charge storage, that makes it a potential candidate as an electrode material.

Received 11th May 2023
Accepted 17th August 2023

DOI: 10.1039/d3ra03140c

rsc.li/rsc-advances

1. Introduction

In recent years, extensive use of technological gadgets has increased the energy storage demands manifold. To meet this requirement in multipurpose environments, the researchers are struggling to the maximum extent.[1] In addition, some major obstructions like environmental pollution and massive usage of fossil fuels at large scale have urged the world to think about alternative energy storage equipment for instance, super-capacitors.[2] Supercapacitors have gained immense interest owing to their remarkable features like low maintenance, quick charge–discharge process, excellent cycling performance, significant power characteristics, and eco-friendly attributes.[3] However, low energy density, low electrical conductivity, and less cycling efficiency are major shortcomings that have restricted their practical applications.[4] To improve the performance of supercapacitors, the scientific community is looking for innovative electrode materials. In this context, some 2D materials, for instance, graphene, molybdenum, silica, *etc* combined with transition metal oxides (TMOs), (like oxides of Mn, Ni, Sn, Co, Fe), in the presence of high-concentration electrolytes are considered as quite favourite.[5]

In general, there are three different classes of super-capacitors depending upon their charging/discharging mechanisms, for instance, hybrid capacitors, pseudo-capacitors, and electric double-layer capacitors also known as EDLCs. The EDLCs require carbon constituents such as graphene, carbon fiber, and carbon nanotubes (CNTs), while pseudo-capacitors include TMOs and conductive polymers (CPs).[6,7] Recently, researchers have paid much attention to TMOs such as RuO_2, Fe_3O_4, Co_3O_4, and MnO_2 because of their high storage capability and low developmental cost to make electrochemical devices.[8–11] Hence, these TMOs are considered good candidates for the active component of supercapacitor electrodes. Likewise, graphene is one of the most active components for supercapacitor applications due to its honey-comb-like structure, and high electrical conductivity, resulting in high power density, and low synthesis cost.[11,12] In addition, graphene has attained a lot of interest owing to some of its captivating characteristics that include its lightweight, electrical conductivity, extraordinary mechanical flexibility, and most of all its chemical stability.[13] Hence, graphene is used to increase a variety of

[a]*Centre of Excellence in Solid State Physics, University of the Punjab, Lahore, Pakistan. E-mail: satiq.cssp@pu.edu.pk*

[b]*Physics and Astronomy Department, College of Science, King Saud University, Riyadh, Saudi Arabia*

[c]*Institute of Molecular Physics, Polish Academy of Sciences, Poznań, Poland*

material characteristics when combined in the form of composites, including electrical and optical properties, toughness, stiffness, UV resistance, dietary changes, and barrier properties.[14] However, the re-stacking and accumulation of the graphene throughout the processing prevents the electrolyte ions from entering the center of the fixed graphene and reduces the capacity of the supercapacitors.[15] To outdo this, the scientists have worked on multiple effective techniques to stop agglomeration and re-stacking between graphene sheets. In this context, it is proposed that $Sr_2Ni_2O_5$ can be combined with carbonaceous nanomaterials to enhance electrochemical performance. As a result of the novel design of integrating graphene with $Sr_2Ni_2O_5$, composite electrode materials with a complex formation between graphene sheets and transition metals present immense potential for practical applications.

Additionally, numerous studies concluded that reduced graphene oxide (rGO) based composites show excellent potential for use as electrode material in supercapacitors. For instance, Marand *et al.* (2021) used nickel nitrate and rGO as oxidants, together with thioacetamide with glycine, to develop nickel sulphide/rGO composites using the combustion method. The composite demonstrated pseudo-capacitive behaviour at a current density of 1.1 A g^{-1} followed by a significant specific capacitance value of 305 F g^{-1}. It was also analysed that the strong conductivity and the dispersion of nickel sulphide particles on rGO sheets provided an extraordinary retention rate of capacitance (*i.e.*, 91%) even after 3000 cycles.[2] In another work, $NiFe_2O_4$ nanoparticles and rGO nanoflakes were synthesized by Tamilselvi *et al.* (2022) using a hydrothermal process and it was observed that even after 2000 cycles, the value of specific capacitance at a current density of 1 A g^{-1} was about 599 F g^{-1} followed by an exclusive retention rate of ~86.5%, respectively.[16] Palanisamy *et al.* (2021) developed a composite of MoS_2/Fe_2O_3/G for utilizing it as an electrode material, the composite was synthesized through a hydrothermal process and the major aim was to use this material in supercapacitors. It was observed that the composite electrode showed some remarkable cyclic behaviour by showcasing a high value of specific capacitance *i.e.*, 98.2 mA h g^{-1} corresponding to the current value of 1 A g^{-1}, respectively.[17] A rGO/$NiMoO_4$ composite was manufactured by Muthu *et al.* (2021) *via* a hydrothermal process. The composite electrode demonstrated a capacitance of 74 F g^{-1} as well as an energy density of 26.3 W h kg^{-1} at 0.75 A g^{-1} in the electrode configuration.[18] Qin *et al.* developed a model to study the effect of mass ratio, cell potential window and materials efficiency on the cell performance and observed an energy density of 69.5 W h kg^{-1} and a power density of 450 W kg^{-1} for hybrid supercapacitor cell assembled using solid polymer electrolyte.[19] Yan *et al.* compiled a comprehensive review regarding rationale design of nanostructured electrode materials for supercapacitor applications and elaborated how understanding of crystal structure, morphology, and charge/discharge mechanism helped to improve the electrochemical performance of electrode material in supercapacitors.[20] By taking into account the above-mentioned studies, it can be suggested that hybrid rGO-based composite structures can be effectively employed in supercapacitors to enhance electrochemical performance. In this context, here we develop an efficient $Sr_2Ni_2O_5$/rGO composite electrode for a systematic analysis of its electrochemical performance so that we can propose a material having significant value of specific capacitance and power density, simultaneously.

2. Experimental

2.1 Production of graphene oxide

To achieve the graphene oxide (GO) in the present research work, a modified Hummer's technique was utilized. For this purpose, 2 g of graphite powder was combined with 150 mL purified sulfuric acid (97%) in a 1000 mL beaker and then stirred continuously for 6 h before being left overnight to complete the reaction. The oxidation reaction is an exothermic process, so the modest addition of potassium permanganate could elevate the temperature. Meanwhile, an ice bath was taken and about 16 g of $KMnO_4$ was poured into the mixture and then set aside. This process took 5 h to complete and the temperature was kept below 5 °C. Right after this, 150 mL of deionized water was poured gradually into the mixture and then the whole mixture was stirred in the ice bath for about 2 h. To complete the oxidation process till the colour changes to reddish-brown, the mixture was heated for about 2 h at 80 °C. After removing the mixture from the hot plate and allowing it to cool at room temperature, 15 mL H_2O_2 was poured dropwise unless the mixture turned from reddish brown colour to brilliant yellow-brown, and about 30 min time was utilized by the particles to settle down properly. At a stirring rate of 2100 rpm, the mixture was centrifuged for about 20 min approximately and the GO paste was settled at the bottom of the tubes which was cleaned many times with deionized water to remove the contaminants. After centrifugation, a thick brown paste of GO was formed, and GO flakes were produced by drying the paste in an oven at 80 °C for 6 h. Whereas, the attained GO flakes were carefully poured and used for composite preparation.

2.2 Synthesis of rGO

A solvothermal method was used to reduce GO. For this, 50 mL of 100% ethanol was uniformly mixed with a suitable quantity of GO (which was dispersed in aquatic solution with a concentration of 2 mg mL^{-1}), calcined at 180 °C before being sonicated for 2 h and then finally for a time span of 3 h, it was magnetically stirred at about 70 °C. Furthermore, using a Teflon-coated autoclave of 100 mL, the mixture was heated for about 3 h at 180 °C. High temperature and increased internal pressure both helped to reduce the GO during the procedure. After lowering the temperature of the autoclave to room temperature, the finished product was collected. Following washing and drying, a fine, dark-brown powder was obtained.

2.3 Synthesis of $Sr_2Co_{2-2x}Ni_{2x}O_5$

In this work, a series of $Sr_2Co_{2-2x}Ni_{2x}O_5$ (where $x = 0.0$, 0.33, 0.67, and 1.0) samples was prepared through sol–gel auto-

combustion technique. For this purpose, analytical grade metal nitrates, for instance [$Sr(NO_3)_2$, purity ≥ 99%], [$Co(NO_3)_2 \cdot 6H_2O$, purity ≥ 98%], and [$Ni(NO_3)_2 \cdot 6H_2O$, purity ≥ 98.5%] were used as precursors while urea (CH_4N_2O), and glycine ($NH_4C_2O_2$) were utilized as fuelling agents. In the process, the metal nitrates to fuel agent ratio was kept at 1 : 2 for all the samples. The stoichiometrically calculated weight% of metal nitrates and fuelling agents were dissolved in deionized water in order to achieve a homogeneous and transparent solution. The separate solutions were then mixed in a beaker and placed on a hotplate at 95 °C, placed in an ESCO fume hood. The solution was stirred magnetically for about 4 h at 250 rpm. When the solution was converted into a gel, the stirring was stopped and the magnetic stirrer was taken out of the gel. The temperature was raised in steps to 250 °C. This led to a vigorous exothermic reaction and the gel was burnt to lose and fluffy ashes. An Agate mortar and pestle were used to grind the ashes so that they could be turned into a homogenous powder. For ensuring the crystallinity and removing unwanted ions, the powder samples were thoroughly calcined in a box furnace at 650 °C for 2 h. All the samples were prepared using the same procedure.

2.4 Synthesis of $Sr_2Ni_2O_5$@rGO composites

To make $Sr_2Ni_2O_5$@rGO composites, a solvothermal method was used. Four samples were used as active material, *i.e.*, $Sr_2Ni_2O_5$ and $Sr_2Ni_2O_5$ with 5, 10, and 15 wt% of rGO. For composite synthesis, both phases were mixed in ethanol and the solution was placed in a sonication bath for 1 h. The solution was then magnetically stirred for 4 h. Subsequently, the solution was placed in a Teflon lined autoclave which was then placed in a muffle furnace at 140 °C and the heating process lasted for 5 h. Soon after this heating process, the samples were taken out from the autoclave and washed 3–4 times, and then finally dried in an oven.

2.5 Preparation of electrodes

Electrode preparation proceeded in three steps. 1 × 2 cm pieces of nickel foam (NF) were etched using 37 mL of distilled water having 13 mL of H_2SO_4 dissolved in it making an acidic solution of 50 mL and then ultimately subjected to washing and drying. To make a binding solution, 10 mL dimethyl fumarate (DMF) and 0.2 g polyvinylidene fluoride (PVDF) were taken and for about 30 min with a stirring rate of 150 rpm, the solution was put onto the hot plate to get stirred properly. To make the slurry, a ratio of 8 : 1 : 1 was taken between the active material, binding solution & activated carbon, respectively, wherein, the actual mass of the active material was 0.008 g. Meanwhile, the as-synthesized solution was placed onto a hot plate for 8 h at 450 rpm. The as-synthesized sample was coated on the NF and kept in an oven for 30 min for drying it completely. The coated NFs were used as electrodes of supercapacitors for further characterization. The whole synthesis process of active material and electrode fabrication is depicted in Fig. 1.

3. Results and discussion

In this work, the crystalline phase of the samples was verified through the XRD patterns attained through Bruker D8 advanced X-ray diffractometer having Cu-K_α (λ = 1.54 Å) radiations. For microscopic surface analysis, a Nova NanoSEM-450, field emission scanning electron microscope (FESEM), and scanning tunnelling microscope (STM) were utilized. Furthermore, the energy-dispersive X-ray (EDX) spectroscopy aided by Oxford's instrument was utilized for the compositional study of the samples. All electrochemical properties of $Sr_2Ni_2O_5$/rGO electrodes were studied *via* a 3-electrode cell system except the cyclability test which was carried out in a 2-electrode assembly. The experimental setup involved the deployment of Hg/HgO and Pt foil as the reference and counter electrodes, respectively in a 2 M KOH electrolyte. The electrochemical workstation (CHI 660E) was used to record the cyclic voltammetry (CV) curves, electrochemical impedance spectroscopy (EIS), and galvanostatic charge–discharge curves.

3.1. Structural analysis

The XRD patterns of synthesized $Sr_2Co_{2-2x}Ni_{2x}O_5$ samples having composition (x = 0.00, 0.33, 0.67 and 1.0, respectively), with 2θ values ranging between 15–75° are depicted in Fig. 2. It was observed that for x = 0.00 composition, the intensity peaks were identified corresponding to the (141), (051), (042), (161), (202), (260), (143), and (341) crystal planes, which were determined using an analytical approach as described by B. D. Cullity.[21] The diffraction analysis confirmed the orthorhombic crystal structure of the sample with x = 0.00, as all the peaks were matched well, with the reference ICSD # 00-034-1475, having $Fd\bar{3}m$ space group symmetry, which is a characteristic reference pattern of $Sr_2Co_2O_5$. The existence of contamination-free diversion peaks and the maximum intensity peak seemed around 32.40° denoting to (141) plane accrediting to the progress of the highly crystalline nature. Upon Ni-substitution (for x = 0.33, 0.67, and 1.0), some new peaks started emerging, which gradually increased in intensity as the Ni-contents were increased in the series. Some intensity peaks also shifted to a different degree, with simultaneous changes in intensity, thus confirming the phase transformation. For x = 1.0, all the intensity peaks were matched with the ICSD # 00-028-1242, which is a characteristic reference pattern of $Sr_2Ni_2O_5$, exhibiting a hexagonal crystal structure.

The prepared samples had principal peaks, as well as several minor peaks, as evident in the XRD patterns. A small deviation in the peaks was caused by the scattering angle that got bigger at larger angles. As a result, a progressive destructive interference occurred to disperse the intensities which was why, the peak intensities at higher angles fell downward. The XRD patterns of all four specimen showed a phase transformation with shifting of peaks.[22] The fine crystalline nature and pure form of the material is described using the high-intensity of the diffraction peaks. Therefore, an evident change in the crystalline structure of $Sr_2Co_{2-2x}Ni_{2x}O_5$ series of samples was observed by the gradual substitution of Ni at the

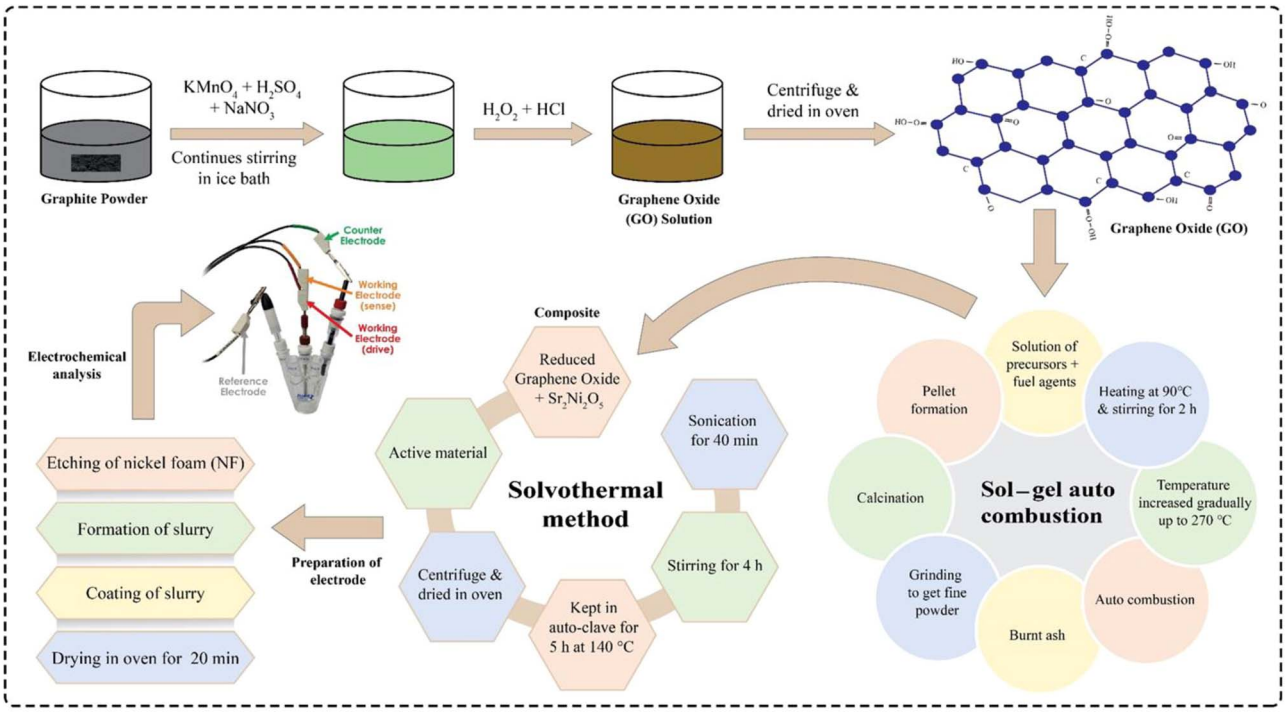

Fig. 1 Schematic profile of sample synthesis.

Co-site. The data obtained from diffraction analysis was subjected to Rietveld's refinement, as illustrated in Fig. 2(b)–(e) having a slight difference in the difference plot that indicates the proper development of the desired phase. Whereas, the value of goodness of fit was closer to 2.00, indicating that the data from the prepared samples was highly in accordance with the reported XRD data. This also confirmed that $Sr_2Ni_2O_5$ was the most crystalline and structurally stable compound as it showed the least value of good fit. This was the reason that $Sr_2Ni_2O_5$ was further utilized for composite formation using rGO for electrochemical analysis. Table 1 is a list of Rietveld's refined structural parameters. Fig. 2(f) provides the XRD patterns of pure $Sr_2Ni_2O_5$, $Sr_2Ni_2O_5$@5%rGO, $Sr_2Ni_2O_5$@10%rGO, and $Sr_2Ni_2O_5$@15% rGO. It is evident from XRD patterns that the intensity of peaks related to the $Sr_2Ni_2O_5$ phase decreases as the rGO contents increase in the composite samples. However, no other peak related to any other phase was seen which confirmed the phase purity of the active material used to make the electrodes.

3.2. Morphological analysis

The FESEM images of $Sr_2Co_{2-2x}Ni_{2x}O_5$ with composition as $x =$ 0.0, 0.33, 0.67, and 1.0, respectively are shown in Fig. 3(a)–(d). The image shown in Fig. 3(a), which is corresponding to

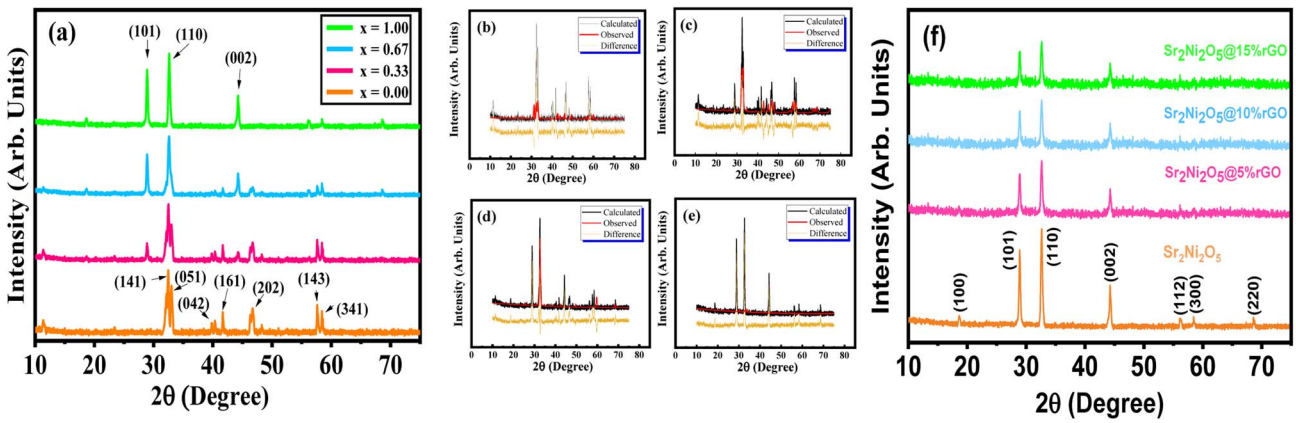

Fig. 2 (a) XRD patterns of $Sr_2Co_{2-2x}Ni_{2x}O_5$, (b–e) Rietveld's refinement, and residual peaks of $Sr_2Co_{2-2x}Ni_{2x}O_5$ ($x = 0.00$, 0.33, 0.67, and 1.00), and (f) XRD patterns of $Sr_2Ni_2O_5$, $Sr_2Ni_2O_5$@5%rGO, $Sr_2Ni_2O_5$@10%rGO, and $Sr_2Ni_2O_5$@15%rGO.

Table 1 Data obtained through Rietveld refinement of the diffraction data

$Sr_2Co_{2-2x}Ni_{2x}O_5$		$x = 0.00$	$x = 0.33$	$x = 0.67$	$x = 1.00$
Cell parameters		$a \neq b \neq c$ (Å)	$a \neq b \neq c$ (Å)	$a \neq b \neq c$ (Å)	$a = b \neq c$ (Å)
		$a = 3.84$, $b = 3.90$, $c = 20.25$	$a = 3.84$, $b = 3.93$, $c = 20.37$	$a = 3.34$, $b = 16.98$, $c = 3.97$	$a = b = 5.45$, $c = 4.07$
Volume $(Å)^3$		303.26	314.61	225.15	120.88
$\alpha = \beta = \gamma$		$\alpha = \beta = \gamma = 90°$	$\alpha = \beta = \gamma = 90°$	$\alpha = \beta = \gamma = 90°$	$\alpha = \beta = 90°$, $\gamma = 120°$
Atomic position					
O	$x \neq y \neq z$	$x = 0.04$, $y = 0$, $z = 0.19$	$x = 0.04$, $y = 0$, $z = 0.19$	$x = 0.00$, $y = 0.55$, $z = 0.25$	$x = 0.00$, $y = 0.31$, $z = 0.25$
O′	$x \neq y \neq z$	$x = 0.50$, $y = 0.00$, $z = 0.08$	$x = 0.53$, $y = 0.00$ $z = 0.08$	$x = 0.00$, $y = 0.31$, $z = 0.25$	$x = 0.00$, $y = 0.55$ $z = 0.25$
Sr	$x = y \neq z$	$x = y = 0.50$, $z = 0$	$x = y = 0.50$, $z = 0.25$		
Sr	$x = y = z$			$x = 0.00$, $y = 0.16$, $z = 0.25$	$x = 0.00$, $y = 0.16$, $z = 0.25$
Sr	$x = y \neq z$	$x = y = 0$, $z = 0.30$	$x = y = 0$, $z = 0.25$	$x = y = 0$, $z = 0.27$	$x = y = 0$, $z = 0.29$
Co	$x = y \neq z$	$x = y = 0$, $z = 0.10$	$x = y = 0$, $z = 0.10$	0	0
Ni	$x \neq y \neq z$	0	0	$x = 0.00$, $y = 0.43$, $z = 0.25$	$x = 0.00$, $y = 0.43$, $z = 0.25$
***R*-factors (%)**					
R_{exp}		8.34	10.42	16.32	18.35
R_p		5.65	7.35	6.93	6.83
R_{wp}		24.42	25.22	20.65	20.35
$D_{statics}$		14.44	15.67	17.39	18.34
Wt $D_{statics}$		13.98	14.76	13.02	21.22
χ^2		2.92	2.42	1.26	1.10

$Sr_2Co_2O_5$ composition, revealed some well-shaped morphology; but mostly large-sized particles with sufficient amount of porosity among the grains were also present. This porosity could be quite beneficial to provide maximum active sites for electrochemical reactions. Overall, the particles in this sample were not uniformly distributed but at the same time, they provided ample space for electrochemical reactions. Small particles seemed to be embedded into each other showcasing themselves into large-sized particles, whereas the porosity factor in this composition was high since particles were interwoven but to some specific extents.[23] Fig. 3(b) corresponds to $Sr_2Co_{2-2x}Ni_{2x}O_5$ with $x = 0.33$, which shows that the grains are uniformly attached in the form of layers so voids are less as compared to Fig. 3(a). The porosity of the samples also seems to be reduced compared to pure $Sr_2Co_2O_5$ but the layered structures with uniform particle sizes are quite beneficial for systematic electrochemical reactions. The average size of the particles was observed around 77 nm. The image also showed agglomerations of uniformly shaped small grains. When the Ni substitution was increased to $x = 0.67$, the grain sizes remained almost the same but their distribution became non-uniform. The agglomeration of small grains into large ones was also evident. Due to this agglomeration, mostly spherical-shaped particles appeared as compared to the previous two compositions as shown in Fig. 3(c) which seemingly depicts that the voids in the sample have been lessened. The reason behind the

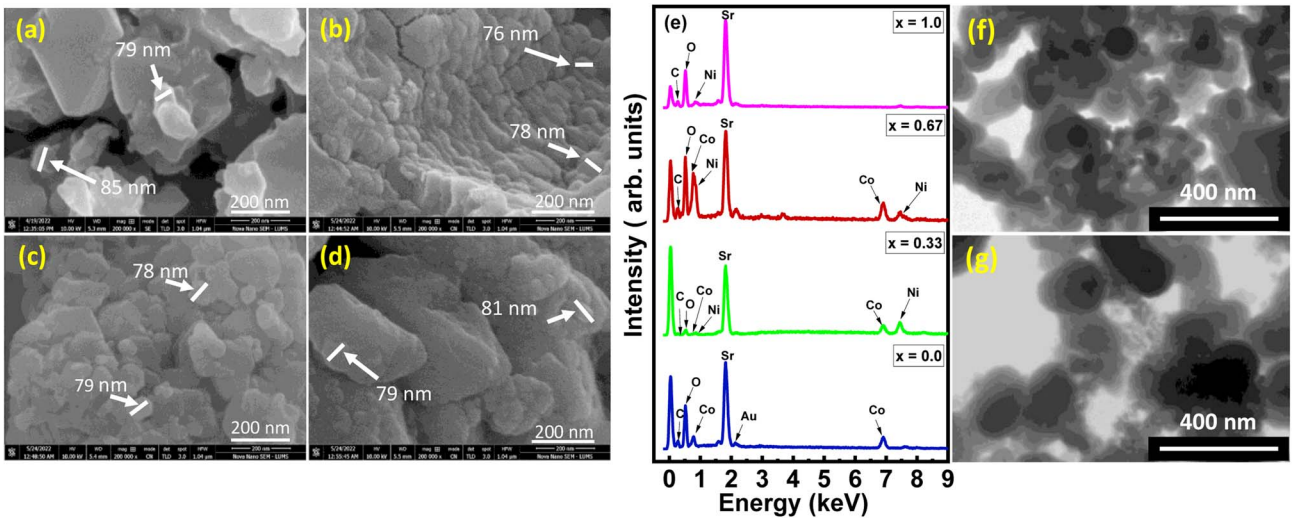

Fig. 3 (a–d) FESEM images, (e) EDX spectra of $Sr_2Co_{2-2x}Ni_{2x}O_5$ ($x = 0.00$, 0.33, 0.67, and 1.00), and STM images of (f) $Sr_2Ni_2O_5$@10%rGO and (g) $Sr_2Ni_2O_5$@15%rGO.

agglomeration of nanoparticles is the weak forces present amongst the particles that cause them to adhere and consequently turn out into micron-sized grains. In addition, covalent or metallic linkages that form in particle clusters cannot be easily broken.

In Fig. 3(d) for composite $Sr_2Co_{2-2x}Ni_{2x}O_5$ at $x = 1.0$, it is analysed that the particles are embedded into each other and the shape of the particles is not uniform so it showed high agglomeration as compared to the previous compositions as shown in Fig. 3(a)–(c) which observed voids in the sample. Fig. 3(a)–(d) also illustrated that the particle sizes were uniform. With several substitutions of x as 0.00, 0.33, 0.67, and 1.00, respectively, it has been seen that particle size varies, progressively. It has been noticed that when the porosity of the sample grows, the grain size of the particles showed fluctuations in size.[24]

3.3. Elemental analysis

Fig. 3(e) illustrates the EDX spectra of $Sr_2Co_{2-2x}Ni_{2x}O_5$ at various concentration levels ($x = 0.00$, 0.33, 0.67, and 1.0), as well as certain peaks of Au and carbon at $x = 0$ and 0.67 so there are no further impurities in the spectra. Typically, the sample is covered with gold to improve the quality of SEM imaging and to eliminate charge deflation, which is the cause of the Au peaks and carbon peaks because of carbon taping.[25] Fig. 3(e) also depicts the elemental composition of all the samples with various changes in substitution. In Fig. 3(e), quite significant peaks of Sr, Co, C along with oxygen O can be viewed with no certain peaks of Ni, which is in accordance with the composition $Sr_2Co_{2-2x}Ni_{2x}O_5$, where $x = 0.0$, that vividly justifies the exact composition of the sample. Wherein by enhancing the substitutional value in Fig. 3(e) for $x = 0.33$, it can be seen there is an obvious peak of Ni, that can be observed at certain energy with % wt of 12.25, whereas minute peaks of Co with % wt of 20.55. At $x = 0.67$ substitution, the EDX spectrum in Fig. 3(e) showed a quite large peak of Co as well as that of Ni which is being taken relatively, compared to the atomic weight percentage of Sr. At $x = 1.0$ substitution, the EDX spectrum in Fig. 3(e), showed that there was no peak of Co whereas Ni had a % wt percentage of 21.84. To summarize, a modest increase in the effective surface area has been found as a result of increased Ni concentration.[26] The elemental composition of $Sr_2Co_{2-2x}Ni_{2x}O_5$ is shown in Table 2. Fig. 4 (f) and (g) shows STM images of $Sr_2Ni_2O_5$@10%rGO and $Sr_2Ni_2O_5$@15%rGO, respectively. These images clearly show the spherical-shaped nature of the particles, having uniform surfaces, with almost the same sizes as determined from FESEM images.

3.4. Electrochemical analysis

To investigate the electrochemical performance, charge storage mechanism, and power density of the prepared electrodes ($Sr_2Ni_2O_5$@rGO), CV, GCD & EIS techniques were employed. In order to evaluate the CV curve, various scan rates associated with a stable potential window of 0.5 V were utilized. The CV loops revealed details about the charge storage mechanism and charge storage capability. Voltammograms of $Sr_2Ni_2O_5$ at scan rates ranging from (5–100 mV s^{-1}) are shown in Fig. 4(a)–(e). The redox peaks during each cycle show that the major capacitance is due to pseudo-capacitive (PCs) behaviour based on faradaic redox reactions. The fact that the symmetry of the peaks was not altered by an intensification in scan rate suggests that the charge storage mechanism has outstanding cyclic reversibility and stability. The polarization effect is responsible for the minute shifting of anodic peaks to the upper potential and cathodic peaks concerning the lower potential. Each voltammogram of this sample reflected clear redox peaks suggesting the fact that in this case, faradaic reactions significantly dominate the performance of the supercapacitors and their trend also shifts them towards the PC nature.[27–29]

The diagrams attribute a significant rate of faradaic and adjustable reactions to the enhanced ionic and automatic charge transport rates that are seen at higher potentials through the amplification of the highest current values associated with an enhanced area of the loop with faster scan rates, respectively. The study revealed that the enhanced area of the loop depicted the enhancement of active positions for charge storage that ultimately enhances its electrochemical performance.[30] Under different scan rates, slight shifting in the redox current peaks to upper and lower potentials are detectable, respectively, confirming electrode resistance and reaction kinetics-controlled reaction processes. The CV curves for the different compositions at a scan rate 0.01 V s^{-1} as shown in Fig. 4(e) demonstrate that the significant capacitance is caused by pseudo-capacitive (PCs) qualities based on faradaic redox processes as indicated by the redox peaks throughout each cycle.[31–33] The nature of the PCs is revealed by all the redox peaks. When associated with rGO in energy storage devices, there are many benefits of using supercapacitors that include the high value of conductivity, stability, large positive specific surface area, and significant electrochemical performance, respectively. From eqn (1), the specific capacitance (SCs) for each composition is calculated.

$$SC = \frac{\int_{V_c}^{V_a} I(V)\mathrm{d}V}{m \times v \times (V_a - V_c)} \quad (1)$$

Table 2 Elemental compositions in $Sr_2Co_{2-2x}Ni_{2x}O_5$

$Sr_2Co_{2-2x}Ni_{2x}O_5$, $x =$	Wt% Sr	Wt% Co	Wt% Ni	Wt% C	Wt% O	Wt% Au
0.0	34.86	27.27	—	5.83	29.7	2.34
0.33	36.86	20.55	12.25	4.93	23.3	2.11
0.67	43.47	19.04	29.46	3.56	4.47	—
1.00	46.85	—	21.84	5.76	25.55	—

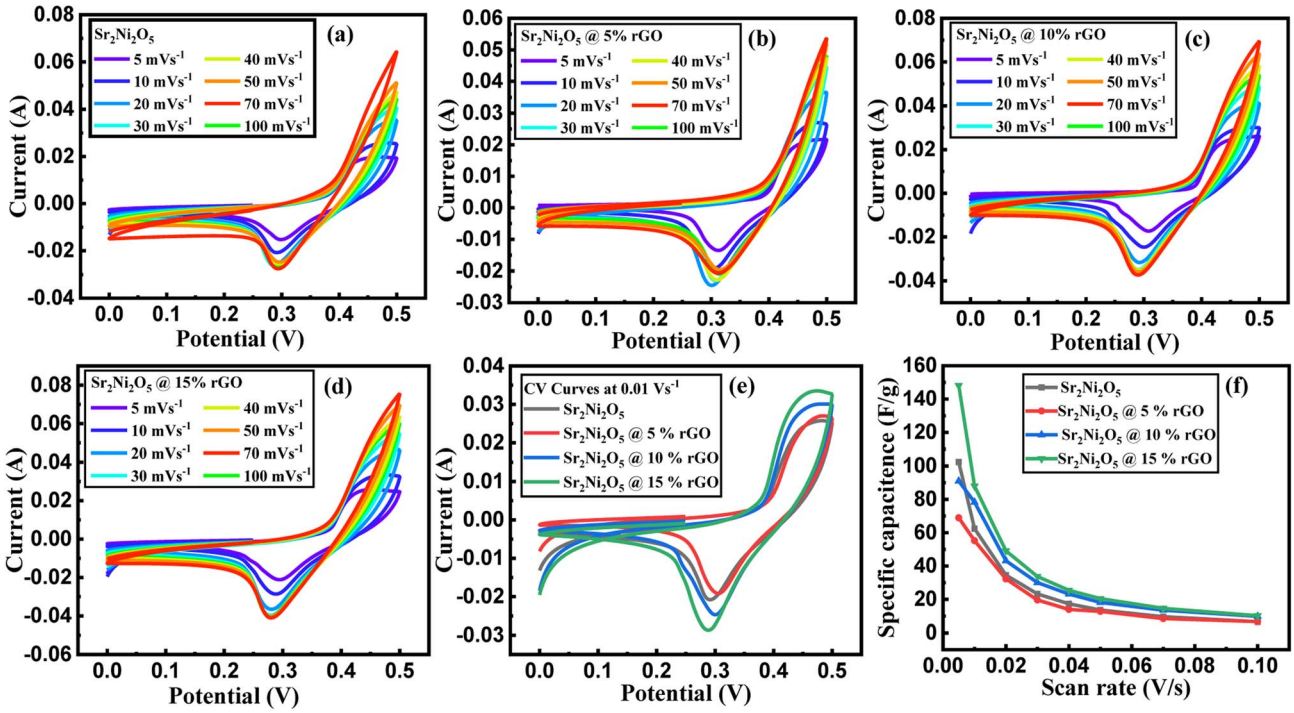

Fig. 4 (a–d) CV curves under numerous scan rates (5–100 mV s^{-1}), (e) combined CV curves at single scan rate of 0.01 V s^{-1}, and (f) specific capacitance *vs.* scan rate for pure $Sr_2Ni_2O_5$, $Sr_2Ni_2O_5$@5% rGO, 10% rGO, and 15% rGO electrodes.

Here ν, I, m, and $(V_a - V_c)$ are the scan rate in V s^{-1}, current in ampere (A), mass measured in grams, and potential window as V, respectively. The SC values for each loop are graphically depicted in Fig. 4(f). Under increased scan rates, a systematic decrease in SC values was observed as expected. Only external types involved in the transference mechanism are in charge of the electrochemical efficiency at greater rates.[34] Table 3 presents the SC values for various composites at different scan rates. It is noted that enhancing the substitution of rGO allows for an increase in specific capacitance. Additionally, among all the composite materials, $Sr_2Ni_2O_5$@15%rGO exhibits the highest specific capacitance. The aforementioned trend implies that the incorporation of rGO into the $Sr_2Ni_2O_5$ results in an enhancement of its charge storage capacity. The increased particular capacitance can be attributed to the unique properties of rGO, such as its high surface area and excellent conductivity. The enhanced specific capacitance demonstrated by $Sr_2Ni_2O_5$@15% rGO implies its viability for efficient consumption in energy storage mechanisms. These findings lead to the understanding of the interactions between rGO substitution and specific capacitance, emphasizing its significance in improving materials compositions to boost electrochemical performance.

Fig. 5(a)–(e) represents the galvanostatic charge–discharge (GCD) curves for $Sr_2Ni_2O_5$ @rGO (5%, 10%, and 15%) samples. The non-linear asymmetric shapes as shown in Fig. 5(a)–(d) demonstrated pseudo-capacitive behaviour, which is as per voltammograms of Fig. 4(a)–(d). The loop area and discharge time depict charge storage capacitance as well as energy and power densities. According to experimental tests, the regular interaction between the activated carbons and the oxide present on the surface is critical for TMO/rGO electrochemical capability when employed as an electrode material for supercapacitors. $Sr_2Ni_2O_5$@rGO nanocomposite demonstrates superior rate capability and stability with respect to other

Table 3 Specific capacitance of pure sample $Sr_2Ni_2O_5$, $Sr_2Ni_2O_5$@5%rGO, $Sr_2Ni_2O_5$@10%rGO, and $Sr_2Ni_2O_5$@15%rGO at different scan rates

Scan rates (V s^{-1})	$Sr_2Ni_2O_5$	$Sr_2Ni_2O_5$@5% rGO	$Sr_2Ni_2O_5$@10% rGO	$Sr_2Ni_2O_5$@15% rGO
Specific capacitance (F g^{-1})				
0.005	68.943	90.958	102.336	148.099
0.01	55.226	78.318	62.421	87.975
0.02	32.299	43.143	34.547	49.098
0.03	19.628	30.089	23.266	33.735
0.04	13.938	23.194	17.320	25.471
0.5	12.813	18.140	13.607	20.460
0.7	8.486	13.539	9.616	14.640
0.1	6.678	9.820	6.573	10.224

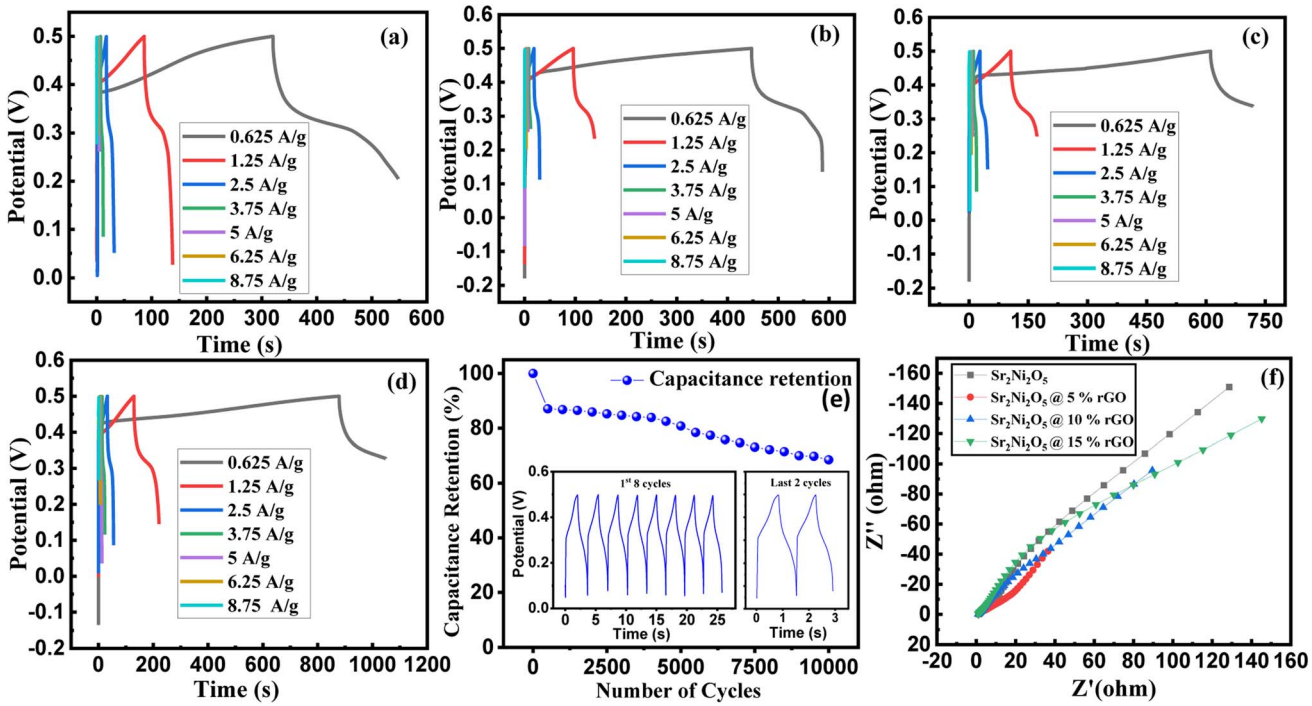

Fig. 5 (a–d) GCD curves at numerous anodic/cathodic currents (5 mA to 70 mA), (e) capacitance retention of $Sr_2Ni_2O_5$@15%rGO after 10 000 cycles, and (f) Nyquist plots for pure $Sr_2Ni_2O_5$ and $Sr_2Ni_2O_5$@5% rGO, 10%rGO, and 15%rGO composites.

physical mixtures. It is worth noting that the presence of graphene ensured excellent cyclic reversibility and the presence of MOs ensured superior capacitance. Overall, the collective immensity of composition is observed. Eqn (2) was used to measure the energy density.

$$E = \frac{1}{2}\frac{SC \times V^2}{3.6} \quad (2)$$

Here, V is potential in this equation. The power density was measured using eqn (3).

$$P = \frac{E \times 3600}{\Delta t} \quad (3)$$

Fig. 5(a)–(d) represents the comparative relation and deep examination of the GCD loops of all the specimens at several current densities. It was examined that the discharge time decreased with the enhancement in current density values for the synthesized electrodes, and this is actually the consequence of the ion diffusion effect, respectively. Presumably, at higher current densities, the connection between the electrolyte and the

Table 4 The specific capacitance at different current densities of $Sr_2Ni_2O_5$, $Sr_2Ni_2O_5$@5%rGO, $Sr_2Ni_2O_5$@10%rGO, and $Sr_2Ni_2O_5$@15%rGO

Sample	Current density (A g^{-1})	Discharge time (s)	Specific capacitance(F g^{-1})	Specific capacitance (C g^{-1})
$Sr_2Ni_2O_5$	0.625	135.659	121.124	84.79
	1.25	46.756	83.492	58.445
	2.5	11.539	41.2107	28.8475
	3.75	4.214	22.575	15.8025
$Sr_2Ni_2O_5$@5%rGO	0.625	174.418	155.7305	109.011
	1.25	68.858	122.9607	86.0725
	2.5	20.264	72.3714	50.66
	3.75	7.818	41.8821	29.3175
$Sr_2Ni_2O_5$@10%rGO	0.625	247.378	220.8730	154.61125
	1.25	94.927	169.5125	118.6587
	2.5	22.942	81.93571	57.355
	3.75	10.345	55.4196	38.7937
$Sr_2Ni_2O_5$@15%rGO	0.625	255.358	227.998	159.598
	1.25	51.72	92.3571	64.65
	2.5	14.549	51.960	36.3725
	3.75	5.24	28.07142	19.65

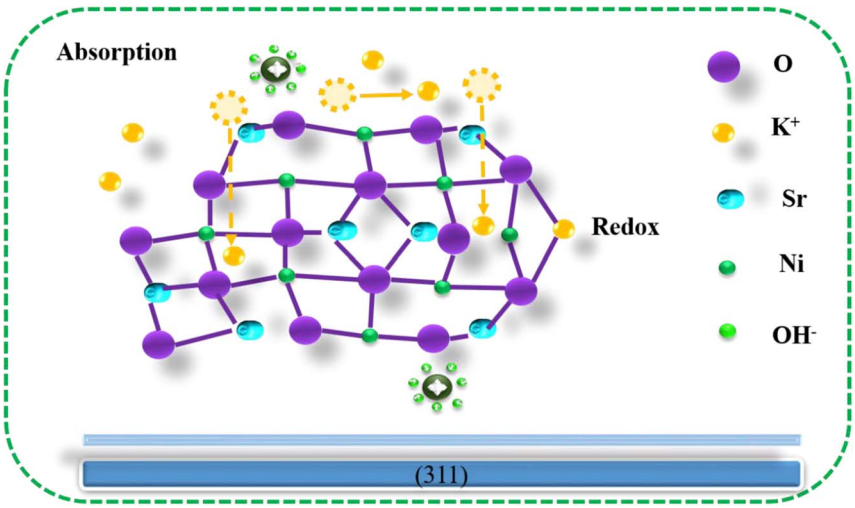

Fig. 6 Charge storage mechanism in $Sr_2Ni_2O_5$@ rGO electrode.

electrode more likely comes to light on the surface and affects a supercapacitor's ability to discharge quickly.[29] Table 4 depicts that $Sr_2Ni_2O_5$@15%rGO electrodes possess remarkable specific capacitance which makes this composition an optimized candidate as electrode material in supercapacitors. To check the cyclic stability, the sample $Sr_2Ni_2O_5$@15%rGO was also tested for 10 000 cycles, as shown in Fig. 5(e). It showed a significant capacitive retention of 68.5% after 10 000 cycles. This test was run at the current density of 5 A g^{-1} and the specific capacitance was 35 F g^{-1} for the first cycle which was reduced to 15 F g^{-1} after 10 000 cycles. Similarly, the energy density value was 4.375 W h kg^{-1} for the first cycle which became 1.875 W h kg^{-1} for the 10 000th cycle, with a maximum power density of 1.25 W kg^{-1}.

The Nyquist plots along with the real (Z') and imaginary (Z'') parts of $Sr_2Ni_2O_5$@rGO (5%, 10%, 15%) compositions are shown in Fig. 5(f). The frequency responses of the electrochemical configurations are illustrated by the impedance profile. The semi-circular region of the graph depicts the high-frequency zone, and the extra-plotted track to the actual axis describes both the high degree of conflict and the electrolyte's ionic resistance. Despite being in the low-frequency region, the plot's linear form indicates how electrolyte ions diffuse and absorb on the electrode surface.[35] The analysis of the data infers that $Sr_2Ni_2O_5$@rGO is quite favourable to be used as electrode constituents in energy-storing devices.

Fig. 6 depicts the $Sr_2Ni_2O_5$@rGO electrode's charge storage method. The initial inclination of K^+ (potassium) atoms is to exist on the dynamic positions of $Sr_2Ni_2O_5$ with low weightage of K^+ contents, taking into account the $Sr_2Ni_2O_5$ charge storage mechanism. At the active sites of $Sr_2Ni_2O_5$ over the preferred (311) plane along low K^+ substances, the engagement of K^+ contents happen positively. On the surface of the $Sr_2Ni_2O_5$, a redox reaction occurs as part of the electrochemical process, changing the valence of Ni. Surface redox pseudo-capacitor behaviour is recognized as the cause of such advancement. The electrode experiences stable electrochemical performance as a result of the aforementioned reaction. Similar to this, the porous nanostructure of $Sr_2Ni_2O_5$ allows for the phenomena of adsorption and desorption of OH^- on the surface. On the electrode's exposed surface, there is a double-layer energy storage behaviour present. The ions that have already been absorbed further disperse on the electrode surface, creating room for new ions to begin adhering. The K^+ atoms migrate from the surface to the subsurface before entering the bulk. The increase in capacity causes the voltage to drop throughout the charge–discharge operation. The K^+ atom adsorption is what causes $Sr_2Ni_2O_5$ to have an electrochemical pseudo-capacitor.[9] Due to the dominant surface capacitive charge storage, $Sr_2Ni_2O_5$@rGO electrodes produce remarkable electrochemical results.

4. Conclusion

To overcome the energy crisis, $Sr_2Ni_2O_5$/rGO a novel electrode composite was synthesized *via* a solvothermal technique using $Sr_2Ni_2O_5$ with rGO (0, 5, 10, and 15% wt) followed by a three-step procedure of electrode fabrication. XRD confirmed the structural analysis as the phase variation of the samples from orthorhombic to hexagonal structure when the substitution contents were enhanced from (x = 0.0 to 1.0) indicating the purity of synthesized material. The surface morphology obtained from FESEM images concludes the porous nature with spherical and arbitrary structure of the particles distributed in multiple dimensions with increasing Ni concentration, the porosity increased. EDX confirmed the perfect stoichiometric ratios of the elemental composition of the prepared samples. Electrochemical analysis curves revealed pseudo-capacitive tendencies of samples while the contribution of surface species in the high scan rates demonstrated a substantial decrease in SC values with maximum SC value of the material $Sr_2Ni_2O_5$@15%rGO of 148 F g^{-1}. This composition revealed 68.5% of capacitive retention after 10 000 cycles. From GCD curves of device the energy density value was noted as 4.375 W h kg^{-1} for the first cycle which reduced to 1.875 W h kg^{-1} for the 10 000th cycle. Conclusively, $Sr_2Ni_2O_5$

with 15% rGO exhibited excellent potential applications in energy storage devices as productive electrode material.

Conflicts of interest

The authors declare no conflicts of interest for this submission.

Acknowledgements

The authors would like to acknowledge the Researchers Supporting Project number (RSP2023R71), King Saud University, Riyadh, Saudi Arabia.

References

1 O. Karaman, I. A. Kariper, S. Korkmaz, H. Karimi-Maleh, M. Usta and C. Karaman, Irradiated rGO electrode-based high-performance supercapacitors: Boosting effect of GO/rGO mixed nanosheets on electrochemical performance, *Fuel*, 2022, **328**, 125298.

2 N. A. Marand, S. M. Masoudpanah, S. Alamolhoda and M. S. Bafghi, Solution combustion synthesis of nickel sulfide/reduced graphene oxide composite powders as electrode materials for high-performance supercapacitors, *J. Energy Storage*, 2021, **39**, 102637.

3 J. Liu, X. Chen, Y. Zhu, R. Chen and W. Yuan, $NiCo_2S_4$/nitrogen and sulfur dual-doped three-dimensional holey-reduced graphene oxide composite architectures as high-rate battery-type cathode materials for hybrid supercapacitors, *Vacuum*, 2021, **190**, 110302.

4 Y. Sun, Z. Li, J. Zhang, S. Ye, R. Hu, F. Zhou and J. Song, Bi_2O_2Se nanosheets/reduced graphene oxide composites for all-solid-state flexible asymmetric supercapacitors with enhanced stability, *J. Solid State Chem.*, 2021, **303**, 122487.

5 M. Vandana, S. Veeresh, H. Ganesh, Y. S. Nagaraju, H. Vijeth, M. Basappa and H. Devendrappa, Graphene oxide decorated SnO_2 quantum dots/polypyrrole ternary composites towards symmetric supercapacitor application, *J. Energy Storage*, 2022, **46**, 103904.

6 E. Somesht and T. Demappa, Tailoring of ternary nanocomposite films of poly(vinyl alcohol)/$AgAlO_2$ @ reduced graphene oxide : An active material for flexible supercapacitors, *J. Solid State Chem.*, 2022, **309**, 122824.

7 Y. Jing, W. Li, D. Wang, X. Chang, M. He and Z. Ren, B-site regulated bimetallic perovskite fluoride $NaCo_{1-x}Ni_xF_3$/reduced graphene oxide as the enhanced performance electrode material for supercapacitors, *J. Alloys Compd.*, 2022, **905**, 164188.

8 T. Uzzaman, S. Zawar, M. T. Ansar, S. M. Ramay, A. Mahmood and S. Atiq, Electrochemical performance of $NiFe_2O_4$ nanostructures incorporating activated carbon as an efficient electrode material, *Ceram. Int.*, 2021, **47**(8), 10733–10741.

9 A. S. Mughal, S. Zawar, M. T. Ansar, F. Afzal, G. Murtaza, S. Atiq and S. M. Ramay, Efficient electrochemical performance of hydrothermally synthesized mixed transition metal oxide nanostructures, *Ionics*, 2022, **28**(5), 2469–2479.

10 J. Azadmanjiri, V. K. Srivastava, P. Kumar, M. Nikzad, J. Wang and A. Yu, Two-and three-dimensional graphene-based hybrid composites for advanced energy storage and conversion devices, *J. Mater. Chem. A.*, 2018, **6**, 702–734.

11 S. Zawar, G. Ali, G. M. Mustafa, S. A. Patil, S. M. Ramay and S. Atiq, $Mn_{0.06}Co_{2.94}O_4$ nano-architectures anchored on reduced graphene oxide as highly efficient hybrid electrodes for supercapacitors, *J. Energy Storage*, 2022, **50**, 104298.

12 S. Rudra, N. Deka, A. Kumar, M. Pradhan and G. K. Dutta, Facile hydrothermal synthesis of Au-Mn_3O_4 decorated graphene oxide nanocomposites for solid-state supercapacitor, *J. Energy Storage*, 2022, **50**, 104615.

13 M. Dashti, E. Kowsari, H. Reza, S. Sarabadani, A. Chinnappan, S. Ramakrishna, N. H. De Leeuw and A. Ehsani, High-performance symmetric supercapacitor based on new functionalized graphene oxide composites with pyrimidine nucleotide and nucleoside, *J. Mol. Liq.*, 2022, **348**, 118381.

14 C. Hsiao, C. Lee and N. Tai, Reduced graphene oxide/oyster shell powers/iron oxide composite electrode for high performance supercapacitors, *Electrochim. Acta*, 2021, **391**, 138868.

15 F. Mahdi, M. Javanbakht and S. Shahrokhian, In-site pulse electrodeposition of manganese dioxide/reduced graphene oxide nanocomposite for high-energy supercapacitors, *J. Energy Storage*, 2022, **46**, 103802.

16 R. Tamilselvi, G. S. Lekshmi, N. Padmanathan, V. Selvaraj, O. Bazaka, I. Levchenko, K. Bazaka and M. Mandhakini, $NiFe_2O_4$/rGO nanocomposites produced by soft bubble assembly for energy storage and environmental remediation, *Renewable Energy*, 2022, **181**, 1386–1401.

17 R. Palanisamy, D. Karuppiah, S. Venkatesan, S. Mani, M. Kuppusamy, S. Marimuthu, A. Karuppanan, R. Govindaraju, S. Marimuthu, S. Rengapillai, M. Abdollahifar, A. K. Anbalagan and R. Perumalsamy, High-performance asymmetric supercapacitor fabricated with a novel MoS_2/Fe_2O_3/Graphene composite electrode, *Colloid Interface Sci. Commun.*, 2022, **46**, 100573.

18 D. Muthu, S. Vargheese, Y. Haldorai and R. T. Rajendra Kumar, $NiMoO_4$/reduced graphene oxide composite as an electrode material for hybrid supercapacitor, *Mater. Sci. Semicond. Process.*, 2021, **135**, 106078.

19 Q. Qin, D. Ou, C. Ye, L. Chen, B. Lan, J. Yan and Y. Wu, Systematic study on hybrid supercapacitor of Ni-Co layered double hydroxide//activated carbons, *Electrochim. Acta*, 2019, **305**, 403–415.

20 J. Yan, S. Li, B. Lan, Y. Wu and P. S. Lee, Rational design of nanostructured electrode materials toward multifunctional supercapacitors, *Adv. Funct. Mater.*, 2020, **30**(2), 1902564.

21 R. Ashwini, V. G. Dileepkumar, K. R. Balaji, R. Viswanatha, C. R. Ravikumar, C. Srivastava and M. S. Santosh, Ternary alkali metal chalcogenide engineered reduced graphene oxide (rGO) as a new class of composite ($NaFeS_2$-rGO) and its electrochemical performance, *Sens. Int.*, 2021, **2**, 100125.

22 A. Paul, S. Ghosh, H. Kolya, C. W. Kang, N. Chandra Murmu and T. Kuila, Synthesis of nickel-tin oxide/nitrogen-doped reduced graphene oxide composite for asymmetric supercapacitor device, *Chem. Eng. J.*, 2022, **443**, 136453.

23 L. Li, J. Chen, H. Gao, F. Liu, Z. Li, Q. Li and J. Zhang, Hierarchical sandwich NiFe layered double hydroxide/reduced graphene oxide for high energy density asymmetric supercapacitors, *J. Electroanal. Chem.*, 2022, **907**, 116065.

24 S. Mojtahedi, M. Serrapede, A. Lamberti, C. F. Pirri, E. Heydari-Bafrooei, M. Molaei and M. Karimipour, A facile, safe and controllable morphology synthesis of rGO_Cu_2O nanocomposite as a binder-free electrode for electrochemical capacitors, *Electrochim. Acta*, 2021, **390**, 138856.

25 Z. Shi, G. Sun, R. Yuan, W. Chen, Z. Wang, L. Zhang, K. Zhan, M. Zhu, J. Yang and B. Zhao, Scalable fabrication of $NiCo_2O_4$/reduced graphene oxide composites by ultrasonic spray as binder-free electrodes for supercapacitors with ultralong lifetime, *J. Mater. Sci. Technol.*, 2022, **99**, 260–269.

26 N. S. Shaikh, S. B. Ubale, V. J. Mane, J. S. Shaikh, V. C. Lokhande, S. Praserthdam, C. D. Lokhande and P. Kanjanaboos, Novel electrodes for supercapacitor: Conducting polymers, metal oxides, chalcogenides, carbides, nitrides, MXenes, and their composites with graphene, *J. Alloys Compd.*, 2022, **893**, 161998.

27 J. Xu, L. Wu, Y. Liu, J. Zhang, J. Liu, S. Shu, X. Kang, Q. Song, D. Liu, F. Huang and Y. Hu, NiO-rGO composite for supercapacitor electrode, *Surf. Interfaces*, 2020, **18**, 100424.

28 S. Huo, W. Ni, Y. Zhao, X. Song, Y. Zhao, K. Li, H. Wang and M. Zhang, Highly efficient atomically dispersed Co-N active sites in porous carbon for high-performance capacitive desalination of brackish water, *J. Mater. Chem. A*, 2021, **9**, 3066–3076.

29 L. Miao, Z. Song, W. Du, X. Zheng, Y. Lv, L. Gan and M. Liu, Advances in organic cathode materials for aqueous multivalent metal-ion storage, *Mater. Chem. Front.*, 2023, **7**, 2731–2749.

30 R. Kumar and R. Thangappan, Electrode material based on reduced graphene oxide (rGO)/transition metal oxide composites for supercapacitor applications: A review, *Emergent Mater.*, 2022, 1–17.

31 S. Chen, D. M. Koshy, Y. Tsao, R. Pfattner, X. Yan, D. Feng and Z. Bao, Highly Tunable and Facile Synthesis of Uniform Carbon Flower Particles, *J. Am. Chem. Soc.*, 2018, **140**, 10297–10304.

32 X. Zheng, L. Miao, Z. Song, W. Du, D. Zhu, Y. Lv, L. Li, L. Gan and M. Liu, In situ nanoarchitecturing of conjugated polyamide network-derived carbon cathodes toward high energy-power Zn-ion capacitors, *J. Mater. Chem. A*, 2022, **10**, 611–621.

33 M. Wang, T. Zhang, M. Cui, W. Liu, X. Liu, J. Zhao and J. Zhou, Sub-nanopores-containing N,O-codoped porous carbon from molecular-scale networked polymer hydrogel for solid-state supercapacitor, *Chin. Chem. Lett.*, 2021, **32**, 1111–1116.

34 Y. Zhao, Y. Mu, L. Wang, M. Liu, X. Lai, J. Bi, D. Gao and Y. Chen, $MnCO_3$-rGO composite anode materials: In-situ solvothermal synthesis and electrochemical performances, *Electrochim. Acta*, 2019, **317**, 786–794.

35 M. B. Askari, P. Salarizadeh, A. Di Bartolomeo and F. Şen, Enhanced electrochemical performance of $MnNi_2O_4$/rGO nanocomposite as pseudocapacitor electrode material and methanol electro-oxidation catalyst, *Nanotechnology*, 2021, **32**, 325707.